Astronomy & Astrophysics manuscript no. paper
March 22, 2017
©ESO 2017

The supernova-regulated ISM III: A comparison of simulated polarization with Planck observations

M.S. Väisälä[1,2], F.A. Gent[2], M. Juvela[1], and M. J. Käpylä[3,2,⋆]

[1] Department of Physics, Gustaf Hällströmin katu 2a, PO Box 64, 00014 University of Helsinki, Finland
e-mail: miikka.vaisala@helsinki.fi
[2] ReSoLVE Centre of Excellence, Department of Computer Science, Aalto University, PO Box 15400, FI-00076 Aalto, Finland
[3] Max Planck Institute for Solar System Research, Justus-von-Liebig-Weg 3, D-37077 Göttingen, Germany

arXiv:1703.07188v1 [astro-ph.GA] 21 Mar 2017

Received XXXX; accepted YYYY

ABSTRACT

Context. The efforts for comparing polarization measurements with synthetic observations from MHD models has previously concentrated on the scale of molecular clouds.
Aims. Here we extend the model comparisons to kiloparsec scales, also taking into account the hot shocked gas generated by supernova activity, and a non-uniform dynamo-generated magnetic field both at large and small scales.
Methods. Radiative transfer calculations are used to model dust emission and polarization on top of the MHD simulations. We compute synthetic maps of column density, polarization fraction, and polarization angle dispersion function and study their dependencies on the key system parameters. These include the large-scale magnetic field and its orientation, the small-scale magnetic field, and the supernova-driven shocks.
Results. Similar filamentary structure of polarization angle dispersion function as seen in the Planck all-sky maps is visible in our synthetic results, although the smallest scale structures are still absent from our maps. The filaments being related to SN driven shock fronts can reliably be ruled out. These filaments can clearly be attributed to the distribution of the small-scale magnetic field. We also find that the large-scale magnetic field influences the polarization fraction in the sense that a strong plane-of-sky mean field will weaken the observed polarization fraction for a given magnetic fluctuation strength. We witness the anticorrelation of polarization fraction and angle dispersion, and the decrease of polarization fraction as a function of column density. We find evidence supporting the view that the magnetic fields in and around molecular clouds are highly coherent and oriented with the ambient mean field in which they are located.
Conclusions. The observed polarization properties and column density are sensitive to the line-of-sight distance over which the emission is integrated. Studying synthetic maps as function of maximum integration length will further help in the interpretation of observations. The large-scale magnetic field orientation influences the observable polarization properties. These effects are difficult to be quantified from observations solely, but MHD models might turn out useful to separate the effect of the large scale mean field.

Key words. ISM: magnetic fields – Polarization – Radiative transfer – Magnetohydrodynamics (MHD) – ISM: bubbles – ISM: clouds

1. Introduction

Magnetic fields are dynamically important constituents of galaxies, playing a major role, e.g., in the star-formation process and controlling the density and propagation of cosmic rays (see, e.g., Beck 2016, and references therein). Imaging them, however, is non-trivial, as indirect observations are required to visualise them, based primarily on dust polarization, Zeeman effect, and synchrotron radiation (see e.g. Klein & Fletcher 2015, and references therein). Because all such methods have strong limitations, interpretation of the data is difficult, especially for the Milky Way, inside of which we reside. This is where radiative transfer simulations combined with numerical models may become useful, bridging the differences between the physical models and the indirect observations (e.g. Ostriker et al. 2001; Falceta-Gonçalves et al. 2008; Pelkonen et al. 2009; Planck Collaboration Int. XX 2015, hereafter PlanckXX).

Planck is a space mission mapping the anisotropies of the cosmic microwave background (CMB, see e.g. Planck Collaboration Int. I 2011). It also has the capability to measure thermal emission and its polarization from dust grains in all bands up to 353 GHz, and particularly with the High Frequency Instrument in the frequency range 100–857 GHz (HFI, see e.g. Lamarre et al. 2010) the foreground dust can be studied. Polarized dust emission and its spatial variations have been mapped with high resolution and sensitivity in a series of papers. Planck Collaboration Int. XIX (2015, PlanckXIX hereafter) study the all-sky dust emission at 353 GHz, and PlanckXX compute the statistics of polarization fractions and angles outside the galactic plane. In Planck Collaboration Int. XXI (2015) thermal dust emission is compared with optical starlight polarization. Planck Collaboration Int. XXII (2015) presents a study of the variation of dust emission as function of frequency in the range 70–353 GHz. For this paper, the most relevant study in this series is the all-sky study of PlanckXIX, as our modelling efforts concentrate on kiloparsec (kpc) scale magnetohydrodynamic (MHD) models including all the three phases (cold, warm, hot) of the interstellar

⋆ This work belongs to the Max Planck Princeton Centre for Plasma Physics framework

medium (ISM), regulated by supernova (SN) activity and subject to a large- and small-scale dynamo instabilities. The major findings of PlanckXIX include the discovery of anti-correlation between the polarization fraction, p, and polarization angle dispersion, S, and the decrease in the maximum polarization fraction, $p_{\max}$, as column density increases.

The efforts for comparing polarization measurements with synthetic observations from MHD models has concentrated on the scale of molecular clouds. For such comparisons, the relevant MHD models normally include the cold and warm phases of the ISM, describe the magnetic field as a uniform background field, and may include artificial flows to enhance the formation of shocks (e.g. Ostriker et al. 2001; Padoan et al. 2001; Bethell et al. 2007; Falceta-Gonçalves et al. 2008; Hennebelle et al. 2008; Soler et al. 2013; Planck Collaboration Int. XX 2015; Chen et al. 2016). Appropriately the Planck data provide high enough sensitivity and resolution for studies at this length scale. In general, a satisfactory agreement between the synthetic and observed dust polarization properties has been found, with the anisotropic and turbulent character of the magnetic field having been identified as the most decisive factor (e.g. PlanckXX). The deduced all-sky polarization properties (PlanckXIX) and those of zoomed-in regions near molecular cloud complexes (PlanckXX) are rather similar, although dynamics of the ISM are known to change drastically between the smaller and larger scale. The similar polarization properties of the all-sky maps and the zoom-in fields are rather surprising, and deserve further attention.

The large-scale dynamics of the ISM in the star-forming parts of spiral galaxies can be described with a three-phase medium regulated by stellar energy input (McKee & Ostriker 1977). By far the dominating energy source to power turbulence at the 100 pc scale is supernova explosions (SNe) (Abbott 1982). SNe bring significant input of thermal and kinetic energy to the ISM. In the solar neighbourhood Tammann et al. (1994) estimate that SNe inject approximately $3 \times 10^{52}\,\mathrm{erg\,kpc^{-2}\,Myr^{-1}}$ thermal energy, which is dissipated mainly as heat into the ISM, but with some 10% converted into kinetic energy (Chevalier 1977; Lozinskaya 1992). In addition to driving expanding shock fronts that interact with each other, the SNe generate bubbles of hot gas near the galactic disk, which as well as the cold ISM and molecular clouds are embedded within the diffuse warm component. The filling factor of the hot gas is small near the galactic midplane but approaches unity in the halo (Ferrière 2001).

In addition to the re-structuring and mixing of the ISM, SN forcing powers the galactic dynamo in the rotating anisotropic galactic disk. Anisotropic turbulence and a non-uniform rotation profile combine to provide the ingredients for the large-scale dynamo instability, leading to the generation and maintenance of magnetic fields dynamically significant on the galactic scale. Along with the mean magnetic field, a strong fluctuating field is also generated. The dynamo processes are intrinsically connected to the three-phase structure of the ISM, so that both the large- and small-scale filling factor and topology are different in various phases and locations of the galactic disk. Recent numerical MHD models have attained sufficient realism to model these processes self-consistently (Gent et al. 2013b; Hennebelle & Iffrig 2014; Kim & Ostriker 2015; Bendre et al. 2015; Evirgen et al. 2017b; Hollins et al. 2017). These developments enable us to study the influence of the three-phase medium, SN shock fronts, and dynamo-generated magnetic fields on the observable properties of dust polarization at large scales.

In this work we study the influence of the three-phase medium and dynamo-generated magnetic fields on the polarization properties of the galactic ISM. We base this on the data produced by the MHD simulations presented in Gent et al. (2013a) and Gent et al. (2013b), and on radiative transfer calculations that are used to model dust emission and polarization on the local galactic plane and over the whole sky.

		max	min
n	$[\mathrm{cm^{-3}}]$	$5 - 8.5$	$7 \cdot 10^{-6} - 2.7 \cdot 10^{-4}$
T	[K]	$7 \cdot 10^{7} - 3 \cdot 10^{8}$	$135 - 311$
B	$[\mu\mathrm{G}]$	$6 - 10$	0
$\bar{B}$	$[\mu\mathrm{G}]$	$4.6 - 5.5$	0
b	$[\mu\mathrm{G}]$	$4 - 7$	0
u	$[\mathrm{km\,s^{-1}}]$	$147 - 549$	0

Table 1: For the 12 snapshots included in the analysis, at intervals of 25 Myr, the ranges of gas number density n, temperature T, total B, mean $\bar{B}$, fluctuating b magnetic field and velocity u.

The paper is organized as follows. In Sect. 2 we describe the tools and methods used in this study. In Sect. 3 we present the simulated polarization results and compare them to the observations of PlanckXIX. In Sect. 4 we consider how the shock and magnetic field affect the interpretation of observations. In Sect. 5, concluding the paper, we discuss the implications of our results and potential for further studies.

2. Methods

2.1. Numerical MHD simulations

In PlanckXX, polarization statistics are compared to MHD simulations, which include cold and warm phases of the ISM. These employ adaptive mesh refinement in a computational cube 50 pc across (Hennebelle et al. 2008), from which an $18^3\,\mathrm{pc}^3$ subset is selected for analysis. Here, we add comparisons to MHD simulations of the ISM, in which the turbulence is driven by SNe (Gent et al. 2013b; Gent 2012, Chapters 8 & 9). In this model the cold and warm phases are produced, as in the two-phase models, through regulation by thermally unstable radiative cooling, but with the addition of a hot phase generated by SN heating.

To capture all the relevant dynamics of the three-phase model, the simulation domain size has to be increased. The grid is $256 \times 256 \times 560$ and spans horizontally 1.024 kpc and vertically ± 1.12 kpc about the galactic midplane. The supernova supersonic forcing naturally generates a highly shocked turbulent flow, so no artificial forcing is applied. Moreover, the interaction of rotation and anisotropic turbulence with the galactic shear flow induces a natural magnetic field through dynamo action.

Note, that the resolution of 4 pc along each side in these simulations without magnetic fields (Gent 2012, Table 5.1) yield a maximum gas number density for the ISM of about $100\,\mathrm{cm^{-3}}$ and the fractional volume of the cold gas is 0.4%. The fractional volume of the warm gas is 60%, with hot gas about 28% near the SN active midplane and increasing to 41.5% elsewhere. With the magnetic field included (Evirgen et al. 2017a) the model fractional volume of the warm gas increases to about 80%, the hot gas being pushed further into the halo, and the cold gas is confined to an even smaller fractional volume. A snapshot of the thermodynamic profile of the model ISM is displayed in Fig. 1 (left), wherefrom the distribution of the different gas phases is evident. Observed densities and those arising from the MHD simulations of Hennebelle et al. (2008) extend to much higher densities and increased fractional volume of cold ISM. The characteristic properties of the MHD simulation data are listed in Ta-

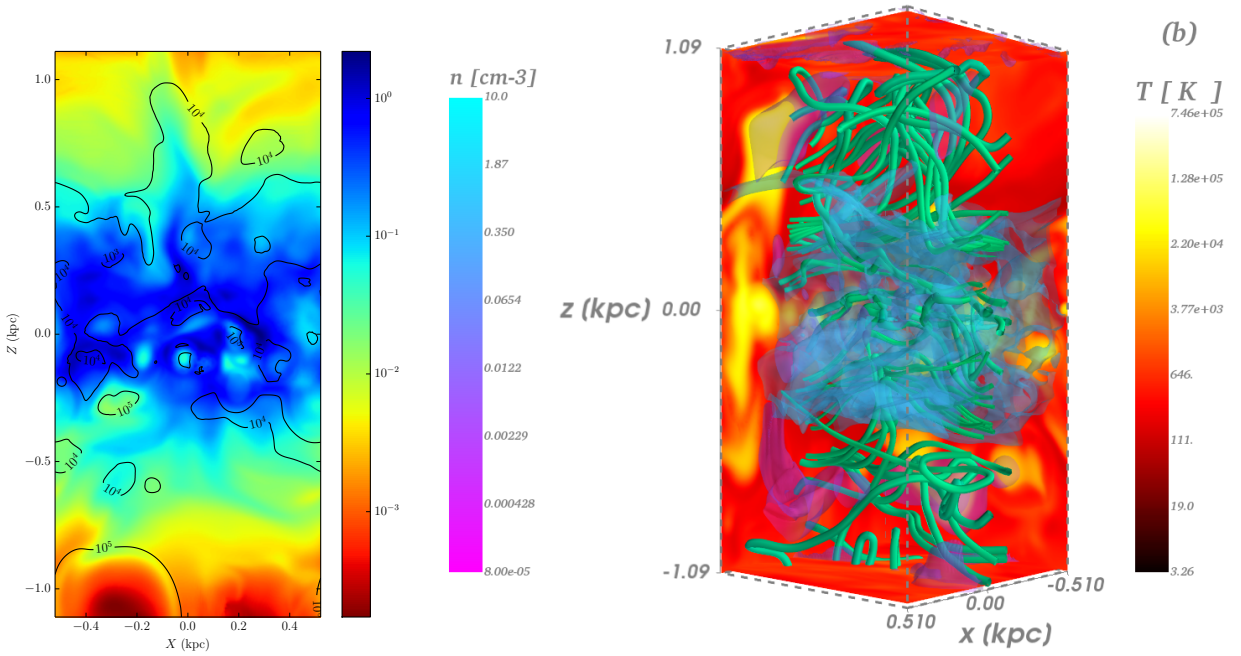

Fig. 1: *Left:* Representative slice in the *xz*-plane of gas number density $n\,[1/\mathrm{cm}^{-3}]$ from a single snapshot overplotted with contours of temperature T [K], illustrates the multi-phase ISM. *Right:* Snapshot of the model ISM, with temperature slices in the background and isosurfaces of the density in the foreground, with fieldlines of the magnetic field over plotted.

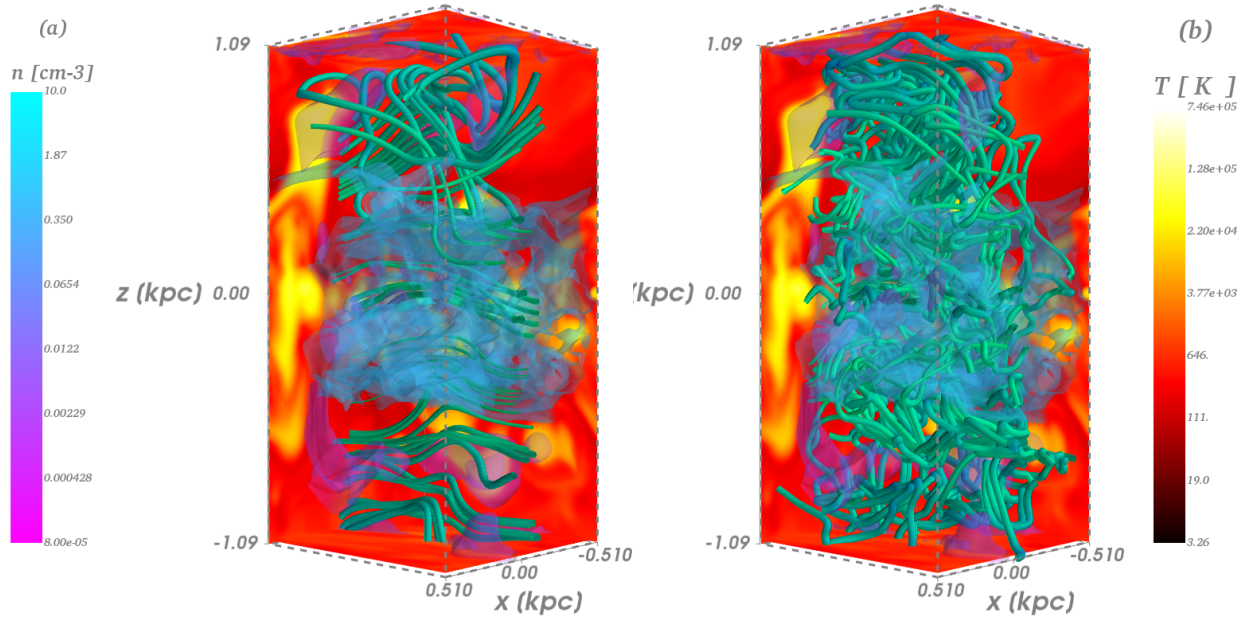

Fig. 2: Snapshot of the model ISM, with temperature slices in the background and isosurfaces of the density in the foreground, as in Fig 1, but with the total magnetic **B** fieldlines replaced by $\bar{\mathbf{B}}$ fieldlines (*left*) and **b** fieldlines (*right*).

ble 1. Temperatures, velocities and magnetic field strengths are better representative of the observed ISM, but smallest scales of their fluctuations are limited by the grid resolution. The saturation of the magnetic field has the effect of restricting the flow and increasing the homogeneity of the ISM, so that the maximum density reduces to about $10\,\mathrm{cm}^{-3}$, which must be taken into account when making comparisons with the Planck observations and the earlier MHD molecular cloud model. Mach number in the simulations reaches as high as 25.

Both large- and small-scale dynamo instabilities are present in the system. A 3D rendition of the magnetic fieldlines embedded in this atmosphere is illustrated in Fig. 1 (right). As reported by Evirgen et al. (2017b), the strength of the generated mean magnetic field at the midplane in the MHD model is in good agreement with the observational estimates of Rand & Kulka-

rni (1989), while the model random field is only 20–50% of the Rand & Kulkarni (1989) estimate or that of Haverkorn (2015). The model and the characteristics of the multi-phase structure of the simulated ISM are described in detail in Gent et al. (2013a). The coherence and fluctuations of the magnetic field are important to the polarization measurements, so it is useful to decompose the field into the mean field $\bar{\mathbf{B}}$ and fluctuations $\mathbf{b}$, where

$$\mathbf{B} = \bar{\mathbf{B}} + \mathbf{b}. \quad (1)$$

We separate $\mathbf{B}$ by volume averaging with a Gaussian kernel (At $l = 50$ pc scale, see Gent et al. 2013b). In Fig. 2 (left) $\bar{\mathbf{B}}$ fieldlines and (right) $\mathbf{b}$ fieldlines are plotted over density isosurfaces on background slices of temperature. Compared to the total field, the mean field computed in this manner is more coherent. It still exhibits spatial structure, which would influence polarization fractions (see Sect. 2.3). The random field is clearly incoherent and would contribute to depolarization.

The gas density ρ from each snapshot is used with the radiative transfer code SOC, (based on Juvela 2005, paper in preparation), to model the dust temperature distribution, and the magnetic field $\mathbf{B}$ is then employed when simulating the dust polarization observations. From the velocity field we can compute directly its divergence, $\nabla \cdot \mathbf{u}$, which is also used in the analysis of the polarization to determine the influence of the shock structure of the ISM on the observations.

The simulation used for this analysis applies parameters for gas density, stellar and dark halo gravitation, galactic rotation, and SN rates and distribution matching estimates for the Solar neighbourhood. The magnetic field is amplified for a period exceeding a Gyr by dynamo action from a seed field of a few nG, which then saturates with an average field strength of a few μG. The strength of the mean field portion is consistent with observational estimates, while the random field strength is 2–5 times weaker than estimated. This has some influence on the degree of polarization dispersion in the simulated observations. We use 12 snapshots from the saturated statistical steady stage of the model, each separated by 25 Myr, commencing at 1.4 Gyr. For simulated maps presented in this paper, we use the snapshot at 1.7 Gyr. The system is in a statistical steady state, so individual snapshot characteristics are representative, but strong temporal and spatial differences are also present. For some of the analysis we consider ensemble averages of the snapshots to identify the most persistent structures.

2.2. Stellar radiation field

Dust in the ISM is illuminated by the stellar radiation field. We invert the measurements of the average stellar radiation field in the solar neighbourhood from Mathis et al. (1983) into a distribution of radiation sources, to model the stellar radiation for our radiative transfer model. We then model this radiation with a horizontal density profile (see Gent et al. 2013a, excluding the dark matter component), and emissivity j_ν reflecting the vertical distribution of stars as

$$j_\nu(z) = j_{\nu,0} \exp\left[a_1\left(z_\mathrm{a} - \sqrt{z_\mathrm{a}^2 + z^2}\right)\right]. \quad (2)$$

Here $a_1 = 4.4 \cdot 10^{-14}$ km s^{-2}, $z_\mathrm{a} = 200.0$ pc and j_ν is the emissivity over the spectrum of frequencies ν. The normalization coefficients, $j_{\nu,0}$, are determined to return the expected total intensity J_ν from

$$J_\nu = \frac{V}{4\pi N} \sum_i^{i=N} \frac{j_\nu(z_i, j_{\nu,0} = 1)}{4\pi d} e^{-\tau_i} \quad (3)$$

where $d = \sqrt{z^2 + r^2}$, $V = 2\pi Z_0 R_0^2$ and τ is the optical depth along the line-of-sight (LOS). The distribution is generated using Monte-Carlo method, and it is scaled to match $J_{\nu,\mathrm{Mathis}}$ from Mathis et al. (1983). Using this inversion, we obtain an approximate z-dependent radiation field, which produces reasonable dust temperatures with our radiative transfer simulations.

2.3. Radiative transfer calculations

To calculate the dust emission, we use the program SOC, which is a new Monte Carlo code for continuum radiative transfer calculations (Juvela et al., in preparation). It has been tested against the CRT program (Juvela 2005) and also against several other codes participating in the TRUST[1] benchmark project on 3D continuum radiative transfer codes. The density distribution of the models can be defined with regular or modified Cartesian grids or hierarchical octree grids. In this paper, all calculations employ regular Cartesian grids. In addition to the density field, the program needs a description of the dust grains (i.e. absorption and scattering properties) and of the radiation sources. The program employs a fixed frequency grid to simulate the radiation transport at discrete frequencies, one frequency at a time. The information of the absorbed energy is used to solve the grain temperatures for each cell of the model. The dust model could also include small stochastically heated grains. However, to predict dust emission at submillimetre wavelengths, the calculations are here limited to large grains that are assumed to remain in a constant temperature, in an equilibrium with the local radiation field. Once the dust temperatures have been solved, synthetic images of dust emission can be calculated towards selected directions or, as in the case of the present study, over the whole sky as seen by an observer located inside the model volume.

During the simulation of the internal radiation field, the radiation transport is calculated without taking the polarization into account. However, SOC includes tools to produce synthetic polarization maps. First, the local grain aligment efficiency can be calculated following the predictions of the radiative torques theory (Draine & Weingartner (1996); Pelkonen et al. (2009); PlanckXX). Because our study concentrates on emission from low-density medium, this step can be omitted. The polarization reduction factor p_0 is simply set to a constant value that results in a maximum polarization fraction that is consistent with observations. Second, maps are calculated separately for the Stokes I, Q, and U components, taking into account the local total emission, the local magnetic field direction, and the value of p_0. These data are then finally converted to maps of polarization fraction and polarization angles.

To calculate the polarization within a single cell, we apply the following method. We use the Planck/HEALPix convention for the polarization angle ψ (Planck Collaboration Int. XIX 2015; Planck Collaboration Int. XXI 2015). Within a cell we normalize the direction of the magnetic field,

$$\hat{\mathbf{B}} = \frac{\mathbf{B}}{||B||} \quad (4)$$

and calculate ψ with

$$\psi = \frac{\pi}{2} + \arctan(\hat{\mathbf{B}} \cdot \hat{\phi}, \hat{\mathbf{B}} \cdot \hat{\theta}) \quad (5)$$

where the $\hat{\phi}$ and $\hat{\theta}$ are the directional vectors of the HEALPix coordinate directions. The angle between the magnetic field and

[1] http://ipag.osug.fr/RT13/RTTRUST/

the plane-of-sky (POS) is

$$\cos^2\gamma = 1 - (\hat{\mathbf{B}} \cdot \hat{D})^2, \tag{6}$$

where $\hat{D}$ is the direction of the LOS. Based on the non-polarized emitted intensity of the cell, $I_{\rm orig}$, we get the Stokes components I, Q and U with

$$I = I_{\rm orig}\left[1 - p_0\left(\cos^2\gamma - \frac{2}{3}\right)\right] \tag{7}$$

$$Q = I_{\rm orig} p_0 \cos(2\psi)\cos^2\gamma \tag{8}$$

$$U = I_{\rm orig} p_0 \sin(2\psi)\cos^2\gamma. \tag{9}$$

To match the polarization degrees observed in the PlanckXIX and PlanckXX we set $p_0 = 0.2$.

From the integrated Q and U we can calculate the polarization fractions p and the polarization angle dispersion functions $\mathcal{S}$ over the whole sky. p and $\mathcal{S}$ provide understandable measure for the system properties and allow comparison to previous studies. The polarization fraction is defined as

$$p = \frac{\sqrt{Q^2 + U^2}}{I} \tag{10}$$

and the polarization angle dispersion function (Falceta-Gonçalves et al. 2008; Hildebrand et al. 2009; Planck Collaboration Int. XIX 2015) as

$$\mathcal{S}(\mathbf{r}, \delta) = \sqrt{\frac{1}{N}\sum_{i=1}^{N}\left[\psi(\mathbf{r}) - \psi(\mathbf{r} + \delta_i)\right]^2}, \tag{11}$$

where $\psi(\mathbf{r})$ is the polarization angle in the given position in the sky $\mathbf{r}$ and $\psi(\mathbf{r} + \delta_i)$ the polarization angle at a position displaced from the centre by the vector δ_i. The sum extends over pixels whose distances from the central pixel in the location $\mathbf{r}$ are between $\delta/2$ and $3\delta/2$. As in PlanckXIX, we calculate the dispersion function with:

$$\psi(\mathbf{r}) - \psi(\mathbf{r} + \delta_i) = \frac{1}{2}\arctan(Q_i U_r - Q_r U_i, Q_i Q_r + U_i U_r). \tag{12}$$

In addition, to be comparable with PlanckXIX we apply 1° Gaussian smoothing to our simulated observations, and set $\delta = 30'$ for all calculations of $\mathcal{S}$.

We have calculated our results with several integration distances $R_{\rm max}$, namely $R_{\rm max} = 0.25$, 0.5, 1, 2, 4 kpc, to explore the effect of depth. This was done assuming periodic boundary conditions in the horizontal direction of the computational domain. However, if the boundary is crossed in the vertical direction, the integration stops at that point, as happens in the cases $R_{\rm max} = 2$ and 4 kpc. Note, for our analysis we mask latitudes $|b| > 45°$ from our maps. This more closely reflects the region of the sky where the Planck observations are included in the analysis of PlanckXIX. It also avoids errors for our calculations of $\mathcal{S}$ associated with the North and South poles. To save space, we omit from the figures the case $R_{\rm max} = 0.5$ kpc, but the results are similar to $R_{\rm max} = 1$ kpc.

2.4. Combining data into histograms

In large part the results in this paper are represented using pairwise joint histograms. This allows us both to compare our results directly to the analysis in PlanckXIX and PlanckXX, and separate the snapshot and point-of-view (POV) specific details from the general large scale behaviour.

For histograms, we combine the radiative transfer simulations from all 12 snapshots and for 5 different POV positions in the approximate midplane, specifically from the points (0.5, 0.5, 1.0) kpc, (0.25, 0.5, 1.0) kpc, (0.5, 0.25, 1.0) kpc, (0.75, 0.5, 1.0) kpc and (0.5, 0.75, 1.0) kpc, under the assumption that using the periodic boundary conditions in x- and y-directions should reasonably represent the ISM in the neighbourhood of the Solar System.

The data is combined as follows. From each SOC generated map, i=1-60, separate pairwise histograms are constructed over a common set of 512×512 bins for each comparison, specifically $C_{\rm bin,i}(N_{\rm H}, p)$, $C_{\rm bin,i}(N_{\rm H}, \mathcal{S})$, $C_{\rm bin,i}(p, \mathcal{S})$. Here $C_{\rm bin,i}$ represents the number of counts in a single bin calculated from a single synthetic observation. Then, assuming $C_{\rm bin,i}$ to be lognormally distributed between separate histograms, we calculate the mean and standard deviation over i,

$$\log C_{\rm bin} = \langle \log C_{\rm bin,i}\rangle, \quad \sigma_{\log C_{\rm bin}} = \sigma(\log C_{\rm bin,i}). \tag{13}$$

We include only the bins $C_{\rm bin}$ for which $C_{\rm bin,i} > 0$ for all i. Second, to reduce additional noise, we mask out the elements where

$$\exp(\log C_{\rm bin} - \sigma_{\log C_{\rm bin}}) < 5, \tag{14}$$

resulting the presented composite histograms. Combined histograms which sum up all counts produce comparable behaviour but contain a lot low count noise in the outliers.

The various simulated observations may each exhibit distinct features worthy of further analysis in the future. However, in this study we focus on the general behaviour of the system. Regardless, it should be kept in mind that particularly the filamentary shapes of the polarization angle dispersion $\mathcal{S}$ (See Figs. 7, 5 and 11) do not convert to histograms in an informative way, as the histograms only combine pixel by pixel values.

3. Veracity of simulated polarization

Here we present our results and analysis based on the synthetic observations obtained using SOC with polarization tools on top of our MHD simulations. For our analysis, we use the maps of column densities $N_{\rm H}$, polarization fractions p and polarization angle dispersions $\mathcal{S}$. As discussed in Sect. 2.1, we take (in the figures) as the reference case the 1.7 Gyr snapshot, where the observer is situated in the centre of the computational domain.

The maps of column density resulting from integrating each distance, up to $R_{\rm max} = 0.25$, 2 and 4 kpc from the observer, are shown in Fig. 3, right panels. The dependence of $N_{\rm H}$ on $R_{\rm max}$ is immediately apparent. The most dense regions are situated near the midplane, as would be expected from horizontal averaging of the gas density in the MHD model represented in Fig. 1. However, this is not visible in the map from $R_{\rm max} = 0.25$ kpc, but clear for the higher $R_{\rm max}$. The vertical anisotropy in the latter reflects the temporal upward shift of the disk centre of mass, evident from Fig. 1. Also, density should be near isotropic in the latitudinal direction, because we do not model the galaxy's central bulge nor spiral arms. In a single snaphot, however, local SN bubbles or superbubbles (merging multiple SN remnants) may inject significant anisotropy into the overall density profile. This is clearly

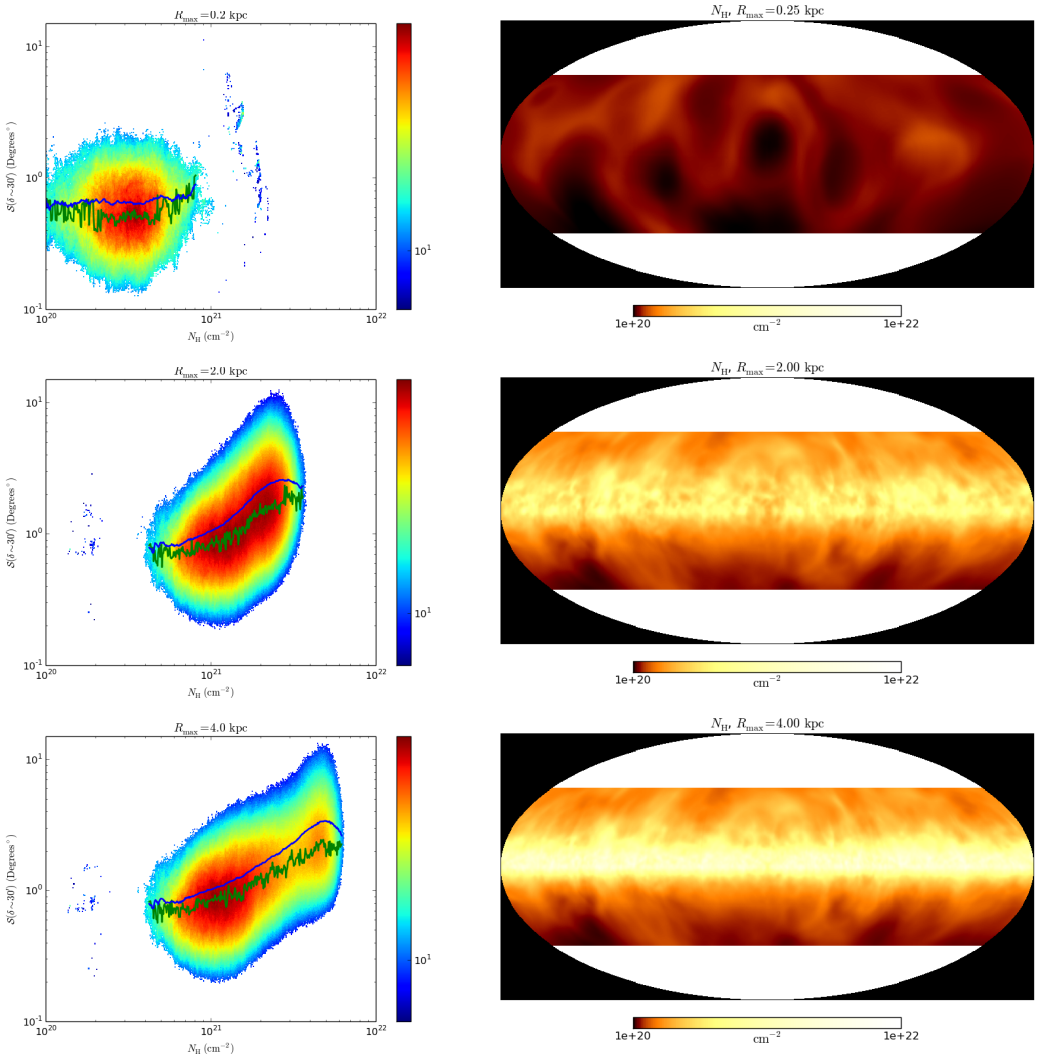

Fig. 3: *Left:* Joint histograms of polarization angle dispersion $\mathcal{S}$ and column density $N_{\rm H}$. The green lines follow the maximum $C_{\rm bin}$ as a function of $N_{\rm H}$, and the blue lines present the weighted mean of $\mathcal{S}$. *Right:* Sample maps of column density. For the case $R_{\rm max} = 1$ kpc, see Fig. 10.

seen only for the $R_{\rm max} < 1$ kpc, with bubbles apparent in several locations. For the higher integration lengths the influence of features near to the observer is almost negligible. Observers have limited control over how measurements relate to the distance of the various sources integrated along each LOS, and thus to determine how properties vary along the LOS. The opportunity to compare and contrast maps based on varying LOS intergration distances with realistic MHD model atmospheres significantly benefits interpretation of observational data.

Fig. 3, left panels, show joint histograms of polarization angle dispersion $\mathcal{S}$ and column density $N_{\rm H}$ from $R_{\rm max} = 0.25$, 2 and 4 kpc. At 0.25 kpc, $N_{\rm H}$ is clustered around only $1.5 \cdot 10^{20}$ cm^{-2} and $\mathcal{S} < 1^\circ$, while its corresponding $N_{\rm H}$ map, dominated by local gas structure, is without dense clouds. For higher $R_{\rm max}$, $N_{\rm H}$ is typically above 10^{21} cm^{-2} and in excellent agreement with the observed column density featured in PlanckXIX, Fig. 24 upper panel. $\mathcal{S}$ also increases above 1, but not to the level obtained by PlanckXIX. The high $R_{\rm max}$ maps of $N_{\rm H}$ also capture the presence of these clouds, particularly evident near the midplane.

On these joint histograms are also plotted lines of maximum $C_{\rm bin}$ (green) and weighted mean (blue) polarization fractions as functions of $N_{\rm H}$. The trend for $R_{\rm max} = 0.25$ kpc is consistent with PlanckXIX Fig. 24, but for $R_{\rm max} \gtrsim 1$ kpc the trend has a positive correlation with $N_{\rm H}$, in disagreement with PlanckXIX. There is no record in PlanckXX on how this relationship applies to their MHD model.

At the lowest $R_{\rm max}$ the visible cloud structure is tracing our MHD model. With increasing $R_{\rm max}$ smaller details appear in the maps, which are projection effects. Hence, the observed results are inevitably a combination of both the MHD model volume and its projection through a mixture of features along the LOS. By assuming periodicity in the horizontal direction, we can reach higher $R_{\rm max}$ than the physical scale of our MHD model. However, with too high $R_{\rm max}$ the periodicity creates a mirror gallery effect of repeating patterns near the x- and y-axis of the MHD model. To avoid this, it is reasonable to restrict the highest integration distance to $R_{\rm max} = 2$ kpc, or for the general case, $R_{\rm max} \lesssim 2L_x$, where L_x is the horizontal extent of the MHD model.

3.1. Polarization fraction across the galactic plane

For each $R_{\rm max}$ we construct joint histograms of polarization fraction p and $N_{\rm H}$, presented in Fig. 4, left panels, and the maps of p,

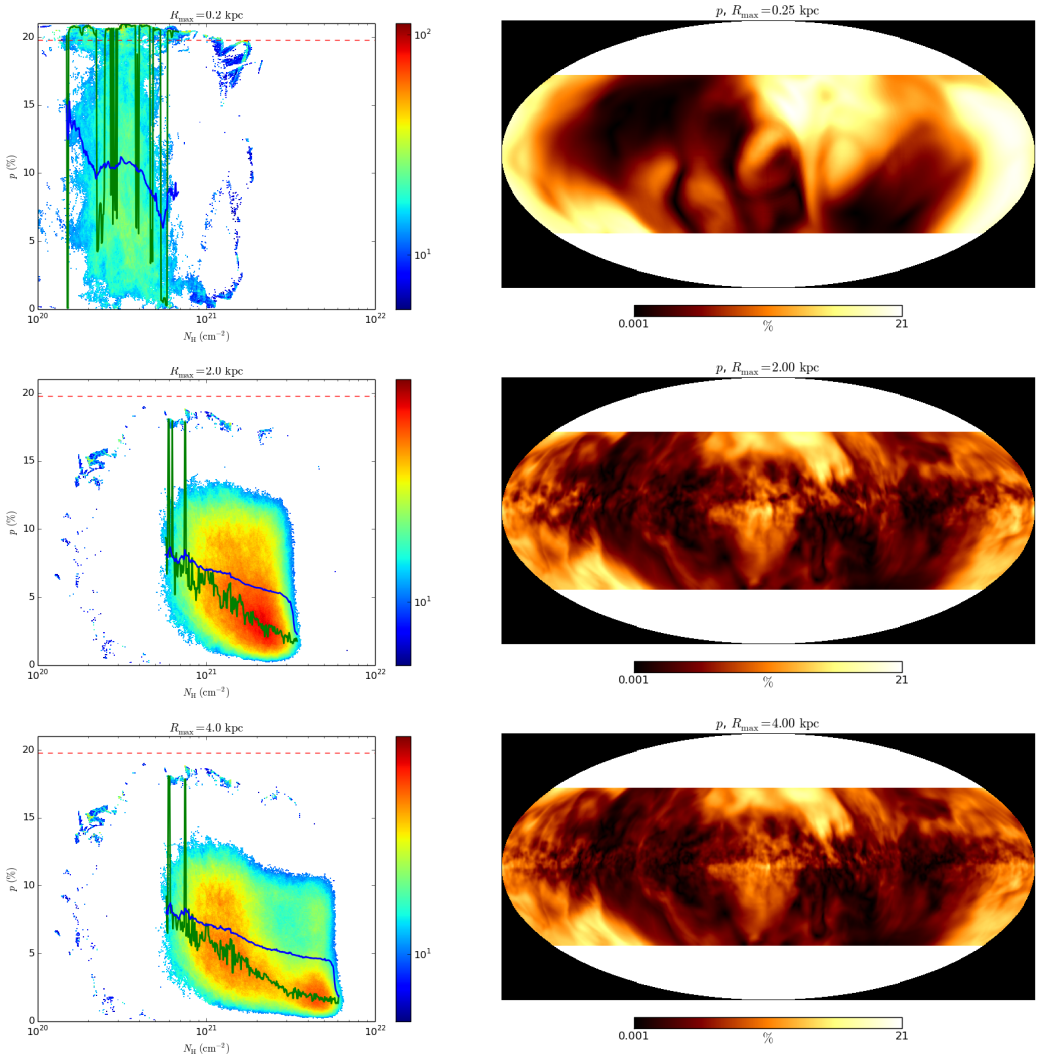

Fig. 4: *Left:* Joint histograms of polarization fraction p and column density N_H. Red dashed lines show the location of $p_{max} = 19.8\%$ from PlanckXIX. The green lines follow the maximum C_{bin} as a function of N_H, and the blue lines present the weighted mean of p. *Right:* Sample maps of p. The polarization fractions are weakened in the galactic midplane, which is seen in the histograms as a growing distribution of low p at high N_H. For $R_{max} = 1$ kpc, see Figs. 11 and 10.

right panels. With $R_{max} = 0.25$ kpc there is a broad range for p values. The distribution extends beyond 20%, above the values observed in PlanckXIX, and is independent of the N_H values, which in our case are much lower than the PlanckXIX observations. From its map p can be seen to be correlated over large smooth regions. There is negligible depolarization, with high C_{bin} appearing on the scale of $p_0 = 20\%$. With $R_{max} = 2$ kpc depolarization is stronger, particularly near the midplane, the p map being an excellent analogue for PlanckXIX, Fig. 6. Its histogram is also a better match with PlanckXIX, Fig. 19, although $N_H > 10^{22}$ cm^{-2} are absent and the are few values with $p > 15\%$. Nevertheless the high densities account for a very small fraction of the PlanckXIX data. The fraction of the PlanckXIX data which has $p > 15\%$ is also tiny. The increased frequency of $p > 5\%$ with $R_{max} = 4$ kpc is more like the PlanckXIX results, but the hight number of points at $p < 5\%, N_H \simeq 5 \cdot 10^{21}$ cm^{-2} are not consistent, and an indication that over sampling the same periodic domain near the midplane is distorting the distribution. To improve the range of column densities in a physically consistent manner, one should increase the horizontal extent of the MHD models. Also, increasing the MHD model resolution would improve both the proportion of high column densities and high polarization fractions.

Regardless of these current limitations, it is interesting to consider how the distances influence polarization and depolarization. Under the framework of the radiative transfer calculations, the mechanism is easy to understand. Along the LOS, individual cells in the grid produce both positive and negative contributions in Q and U, depending on the radiated energy and local direction of magnetic field. For an incoherent magnetic field the sign of Q and U fluctuates, with similar magnitude, such that over very long distances in an optically thin medium their projected totals approach zero. Similarly, in the presence of a directionally coherent magnetic field, its direction will dominate the Q and U over long distances. However, the magnetic fields are highly turbulent throughout the MHD domain, so we expect depolarization to increase with R_{max}.

Near the midplane the depolarization effect is strongly proportional to integration length with $R_{max} \geq 2$ kpc (Fig. 4, lower right panels), corresponding high N_H. This is also consistent with

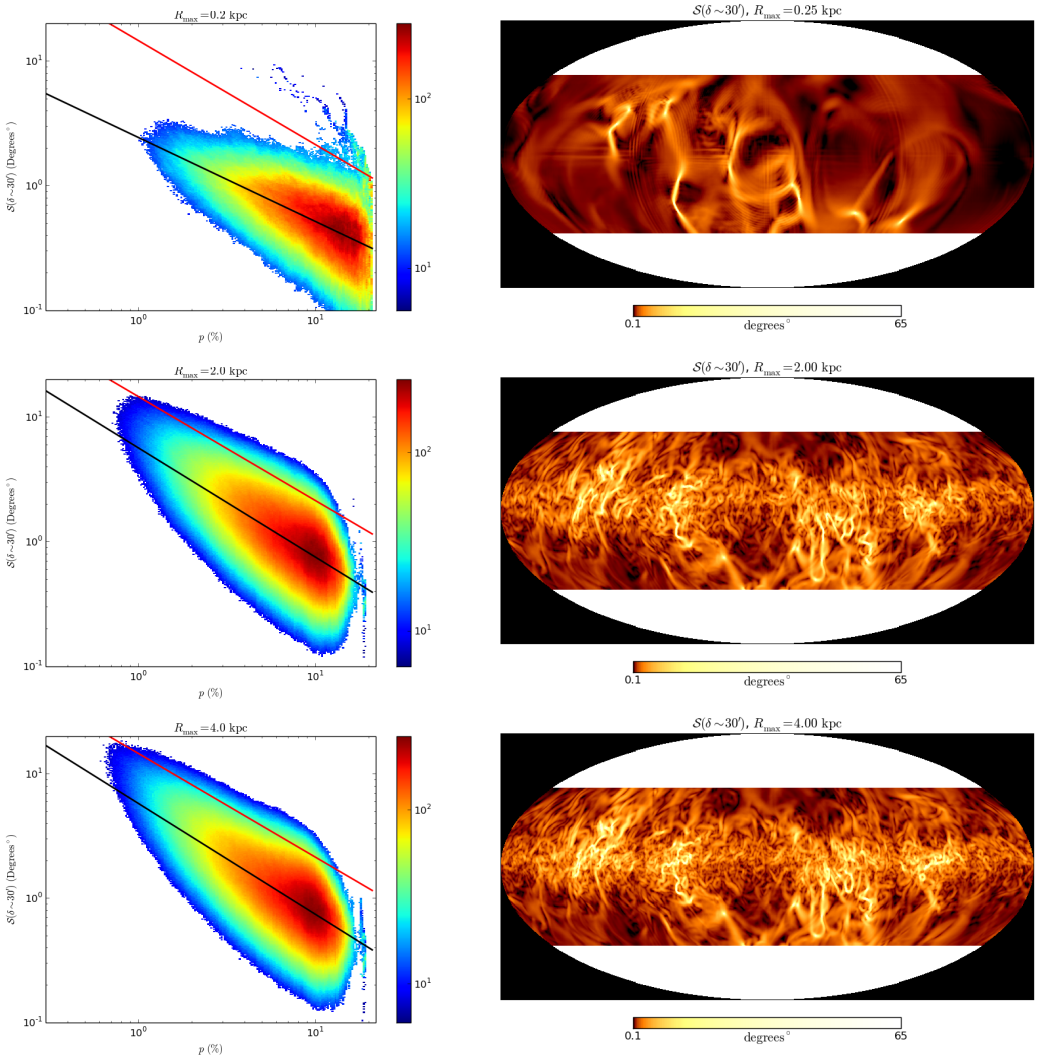

Fig. 5: *Left:* Joint histograms of angle dispersion and polarization fraction, with the effect of increasing $R_{\rm max}$. The red line depicts the fit to the observations as presented in PlanckXIX, $\log_{10}\mathcal{S} = \alpha \log_{10} p + \beta$. The black lines are the best fits to our simulated data, to which α and β are given in the Table 2. *Right:* Sample maps of polarization angle dispersion $\mathcal{S}$ with corresponding $R_{\rm max}$.

the above explanation. Near the midplane with large $R_{\rm max}$ it is possible to integrate polarization over longer distance, unlimited by the upper or lower boundaries of the computational domain. Therefore, there is more influence on p from the depolarizing effect of the fluctuations, most evident near the midplane. The role of magnetic field fluctuations inducing a broad spread of p has also been suggested by PlanckXIX and PlanckXX and our results support this idea. Our findings suggest that the accumulated turbulent fluctuations would at least provide a partial explanation for this effect.

An important difference, however, is that in the MHD simulated observations of PlanckXX which are focussed on local regions representing molecular clouds, the column densities are an order of magnitude lower than the target observations (e.g. PlanckXX their Fig. 17 vs their Fig. 4), similar to our results for $R_{\rm max} = 0.25$ kpc. This demonstrates that our approach of integrating LOS beyond 1 kpc is critical to obtaining realistic simulated observations. Also, in the same experiment their polarization fractions are clustered below 5%, while the target observations more typically have p between 5 – 15%, which supports the hypothesis that magnetic fields in molecular clouds are more coherent than the ISM as a whole and that they are strongly aligned with the ambient warm ISM, in which they are embedded (Gent 2012, Ch. 9 Fig. 9.12). Apparently the artificial forcing in their simulations does not generate a sufficiently coherent field, while the natural evolution of SN driven dynamo naturally induces ordered fields in the intersections between shocks, where clouds tend to form.

Perhaps, here, we also have an explanation for the erroneous positive correlation between $\mathcal{S}$ and $N_{\rm H}$ mentioned in relation to the joint histograms in Fig. 3 with $R_{\rm max} \gtrsim 1$ kpc. Low $\mathcal{S}$ in our simulated observations are associated with low $N_{\rm H}$. With increased integration lengths we recover more regions of high $N_{\rm H}$, and these densities return typical $\mathcal{S} \simeq 3°$ very similar to PlanckXIX with $\mathcal{S} \simeq 4°$. This would be resolved by improved resolution for the MHD model, which would generate higher $N_{\rm H}$ across the spectrum, and correspondingly a distribution of higher $\mathcal{S}$.

Note, that due to the averaging and masking method presented in Sect. 2.4 some of the outlying values can persist as halos in the histograms of Fig. 4 (also Fig. 10), but with higher sampling rates, these masked points in between the bulk data and halo could be restored. Also, a gradual loss of alignment of the dust grains within radiation shielded dense clouds appears to dampen polarization (PlanckXIX). We set the strength of align-

ment proportional to p_0 in Eqs. 7-9, neglecting any effects of such shielding.

3.2. Polarization angle dispersion

Looking at the maps of polarization angle dispersion $\mathcal{S}$ presented in Fig. 5 (right panels), we observe filamentary structures similar in appearance to PlanckXIX Fig. 12. However, for $R_{\rm max} = 0.25$ kpc these are very large scale structures, spanning the full range of examined galactic latitudes in some locations and much thicker than the PlanckXIX observations. As $R_{\rm max}$ increases, the filamentary structure tangles, fragments, increases in number and has more wiggles, quite well resembling PlanckXIX Fig. 12. PlanckXX do not report any filamentary maps of $\mathcal{S}$ from their MHD simulated observations, although their observed target regions show such structures (Fig. 6). As the simulations do not recover such effects, this is likely due to the low integration length of the simulated observations, as with our $R_{\rm max} = 0.25$ kpc, rather than a lack of fluctuations in the MHD model.

$R_{\rm max}$ (kpc)	α	β	$\langle \mathcal{S}/\mathcal{S}_{\rm Planck} \rangle$	Notes
–	**−0.834**	**−0.504**	100%	Planck
0.25	−0.673	−0.961	24%	
0.5	−0.742	−0.898	32%	
1.0	−0.789	−0.920	34%	
1.0	−0.934	−1.020	39%	$2 \cdot \mathbf{b}$
2.0	−0.876	−0.999	35%	
4.0	−0.892	−1.021	35%	

Table 2: Fit coefficients to $\log_{10} \mathcal{S} = \alpha \log_{10} p + \beta$ for each joint histogram of $\mathcal{S}$ and p. The observed values are from the best fit of PlanckXIX.

In Fig. 5 (left panels) the joint histograms of $\mathcal{S}$ and p show some agreement with Fig. 23 of PlanckXIX. Angular dispersion is inversely proportional to polarization fraction, and may be approximated by

$$\log_{10} \mathcal{S} = \alpha \log_{10} p + \beta. \quad (15)$$

The histograms show best fit (black lines) for Eq. (15) and the fit from PlanckXIX (red lines). The parameters are summarised in Table 2. For $R_{\rm max}$ at 1 kpc and above, the gradient of the fit α is near to the PlanckXIX fit, but our histograms are shifted to lower $\mathcal{S}$. The ratio $\mathcal{S}/\mathcal{S}_{\rm Planck} = p^{\alpha-\alpha_{\rm Planck}} 10^{\beta-\beta_{\rm Planck}}$ is averaged and listed in Table 2 for each $R_{\rm max}$. The dispersion values in our simulations increase towards PlanckXIX as $R_{\rm max}$ increases, but plateau at a ratio of 35% for $R_{\rm max} \gtrsim 1$ kpc. The shift is in the opposite direction for PlanckXX comparing their Figs. 19 and 8. Again the slope of the relationship is a reasonable fit, but with high resolution they do obtain a stronger fluctuation field and hence $\mathcal{S}$ is higher. The overshoot is likely accounted for by the incoherence from the artificial forcing. This is further evidence in support of molecular clouds having magnetic fields with significant coherence.

4. Shock and magnetic structure interpretation

We now consider how the filamentary structure of the polarization angle dispersion measurements $\mathcal{S}$ are related to physical properties of the ISM. These are difficult to measure directly through observations, but can be measured easily in the

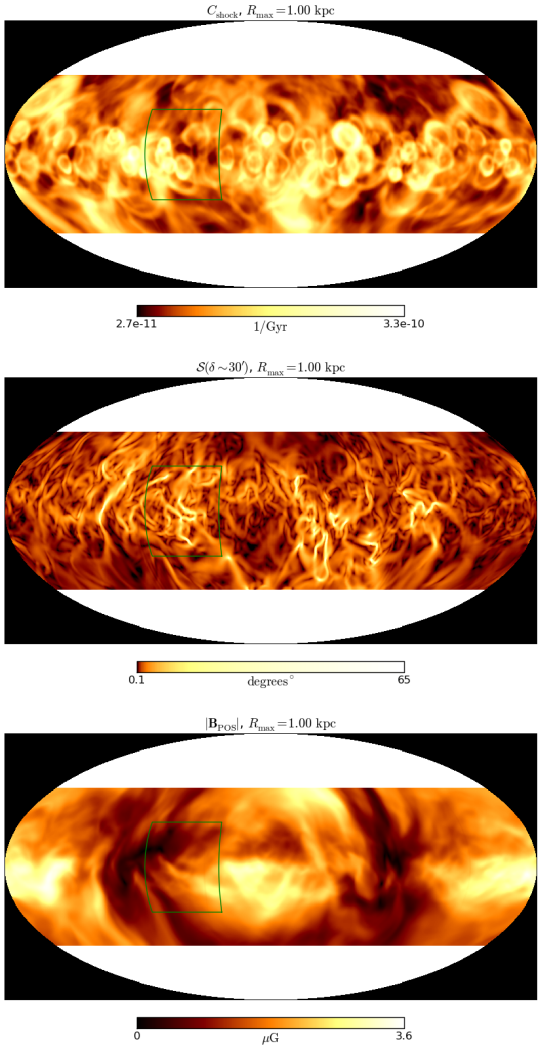

Fig. 6: *Top:* The distribution of the average values of $C_{\rm shock}$ in the LOS. *Middle:* Map of polarization angle dispersion $\mathcal{S}$. *Bottom:* Projected average magnetic field strength in POS. The green rectangles refer to the area featured in Fig. 7. $R_{\rm max} = 1$ kpc.

MHD models. In the analysis that follows, we refer to integration along the LOS with $R_{\rm max} = 1$ kpc. This range is sufficient, within the properties and horizontal extent of the MHD model, to adequately capture the key features present in the PlanckXIX observations. For more demanding analysis it would be recommended to integrate $R_{\rm max} \simeq 2L_x$.

4.1. Shock filament interpretation

Changes in the direction of polarization angle ψ and therefore $\mathcal{S}$ are related to changes in the magnetic field, and these are driven by SNe forced turbulence. Generally, $\mathcal{S}$ follows a lognormal distribution (see PlanckXIX Fig. 14). The lognormal nature of the $\mathcal{S}$ distribution in the observed and simulated ISM is (as explained in Vazquez-Semadeni 1994; Elmegreen & Scalo 2004) consistent with the effect shocked turbulence has on the statistics (as noted in Gent et al. 2013a) of the gas density.

To investigate the effect that the shocks have, we first compute a proxy of their magnitude, $C_{\rm shock} = |[\nabla \cdot \mathbf{u}]_-|$, where only the negative divergence contributes. This corresponds to regions where the flow is *con*vergent, where therefore the shocks cre-

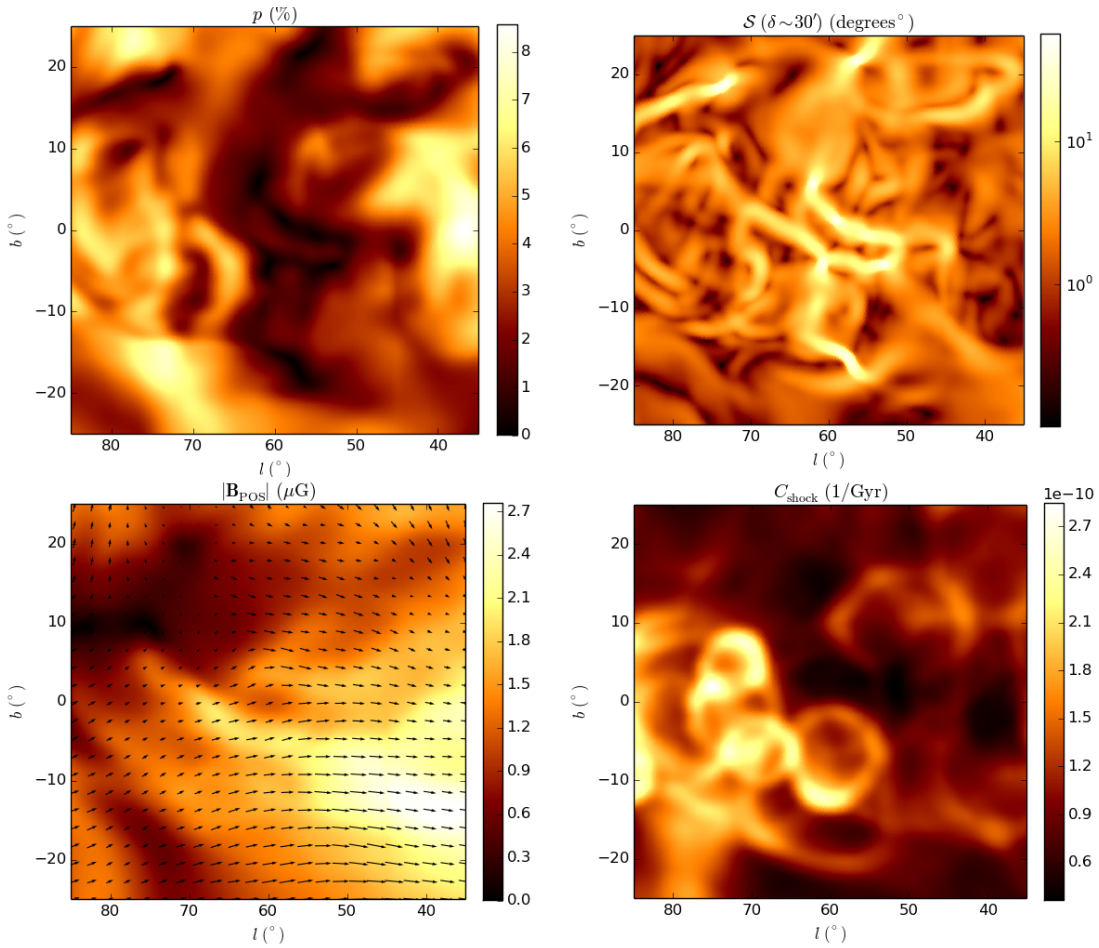

Fig. 7: A local comparison of p, $\mathcal{S}$, $|\mathbf{B}_{\rm POS}|$, and shocks within the area marked in the Figs. 11 and 6.

ated by SNe are compressing the surrounding ISM. In Fig. 6, maps are displayed for average $C_{\rm shock}$, $\mathcal{S}$, and the average POS magnetic field within the LOS integrated over $R_{\rm max} = 1$ kpc. A zoom-in area is marked on each map, for which the local maps are displayed in Fig. 7.

Apart from the energy input to the turbulence being stronger in the midplane due to the general distribution of SNe, there is no visible correlation between the SNe shocks and the average POS magnetic field nor polarization angle dispersion. However, there is a large scale pattern in the magnetic field, which is discussed in the Sect. 4.2.

Examining the zoomed-in area displayed in Fig. 7, the filamentary structures in $\mathcal{S}$ (top right panel) overlap very sharply with the areas of low polarization fraction (top left panel). There is likely a connected phenomenon, which links these effects. Directly relating this to specific physical features in the model is a challenge, because locally the alignment of polarization is a combination of effects layered on the top of each other. One approach to understanding this is to perform a series of calculations over a range of discreet integral lengths $R_{\rm max}$ and to analyse in detail how the maps change as certain features of the model are included or excluded. It is also possible to explore the relationship between magnetic fields and dispersion over large scales.

When comparing the shock profile in Fig. 7 (bottom right panel) with the polarization angle dispersion (top right panel) the strongest filamentary structures correspond to locations where the shocks are negligible. In the upper half of Fig. 7 (bottom left panel) the strength of the POS magnetic field seems to correlate quite well with the polarization fraction (top right panel), however in the lower right quadrant of the map a strong field is anti-correlated to p, so the relationship is not at all straightforward. In principle all of these relationships should be explored further by varying $R_{\rm max}$ as described above, but it appears likely we can exclude the filamentary structure being indicative of the shock structure of the ISM.

4.2. Dispersion and the large-scale magnetic field

The angular dispersion of polarization exhibits a significant dependence on galactic latitude and longitude. This becomes more apparent when taking averages from all simulated observations with the same observer location, but for different snapshots, as is presented in Fig. 8 (lower right panel). The measurements of Q reverse twice in one full rotation in latitude (upper left panel), while U switches sign across the galactic plane and also exhibits the same latitudinal sign reversals as Q (upper right panel). The polarization fractions are minimised where the brightest filamentary structures are most pronounced. The general nature of this pattern may be expected. As outlined in Sect. 2.1, the mean magnetic field is strongly aligned in the direction of the differential rotation of the galaxy.

The latitudinal variation follows from a presence of the mean-field. We can illustrate it with a simple analytical example. Let us assume a simple uniform y-directional mean field with a weak random fluctuation at the smallest scales of the grid

$$\mathbf{B} = B_0\hat{\mathbf{y}} + \Delta\mathbf{b} \tag{16}$$

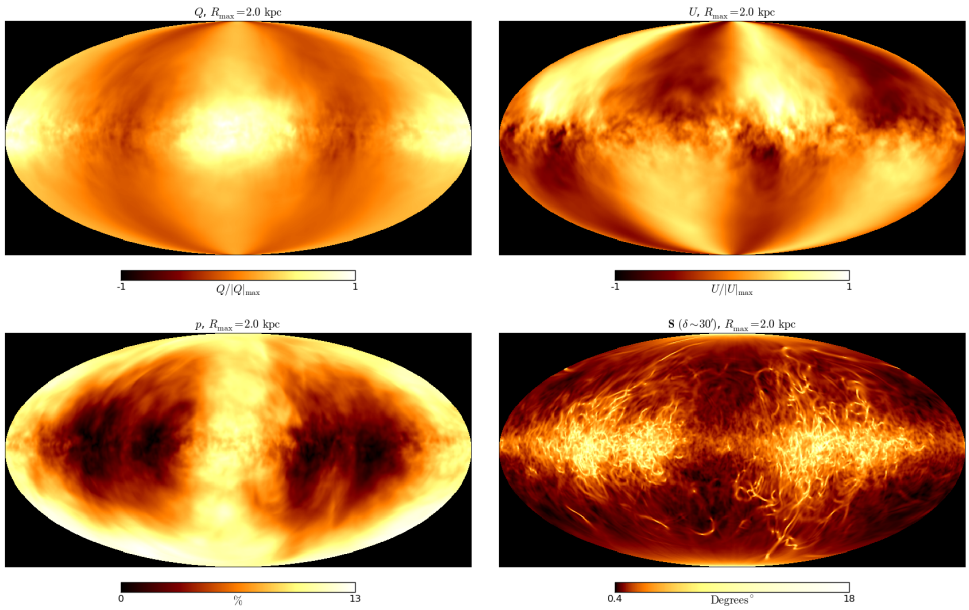

Fig. 8: Averaged maps of Q, U, p, $\mathcal{S}$ over the all 12 snapshots.

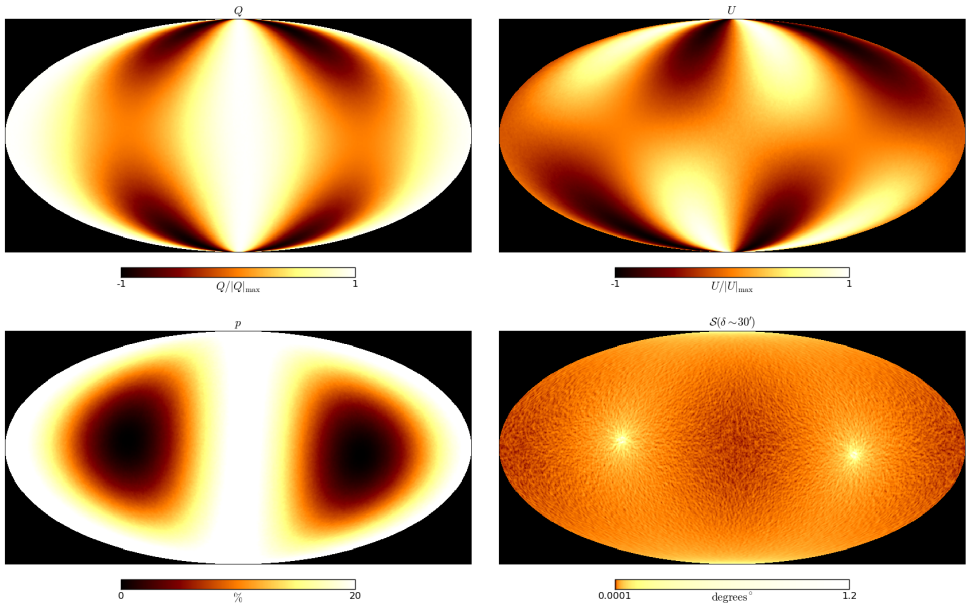

Fig. 9: Distribution of polarization assuming a simple analytical model of the magnetic field as described by the Eq. 16.

where $|B_0\hat{\mathbf{y}}| \gg |\Delta\mathbf{b}|$. This configuration generates a large-scale structure of the polarization (see Fig. 9). In addition to this, the direction of the magnetic field affects the sensitivity of the observed polarization to the small magnetic fluctuations. If we apply Eq. 16 to Eqs. 4, 5 and 6 we notice that near the HEALPix coordinates $\phi \approx \pm\pi/2$ and $\theta \approx \pi/2$ the influence of the magnetic field approaches the values $\psi \approx \pi/2 + \Delta\psi$ and $\gamma \approx \pi/2 + \Delta\gamma$, where we have divided the contribution from the mean and the fluctuating field. Therefore, when calculating the polarization components, with Eqs. 8 and 9, we get,

$$Q \approx -Ip_0 \cos\Delta\psi \sin^2\Delta\gamma \quad (17)$$

$$U \approx -Ip_0 \sin\Delta\psi \sin^2\Delta\gamma. \quad (18)$$

This signifies that, when the LOS approaches the direction of the consistent mean magnetic field, the POS field is highly sensitive to small, local fluctuations caused by turbulence. This in turn will show up as variations in polarization angle and therefore relatively high $\mathcal{S}$. To summarize, when the strong mean field is perpendicular to the LOS, its direction dominates the polarization angles, but when the field is parallel to the LOS, the observed polarization angles are more sensitive to the small fluctuations in the field. However, the polarization fraction p is weak in the mean field aligned with the LOS, as the small fluctuations themselves produce less strong Q and U. Thus, we have a similar interpretation to PlanckXX. In their study, $\mathcal{S}$ is strongest when the POV faces towards the mean-field direction, along with weaker polarization fraction. In contrast, they observe more strong polarization fraction and coherent polarization angle when the direction of the mean field follows the POS.

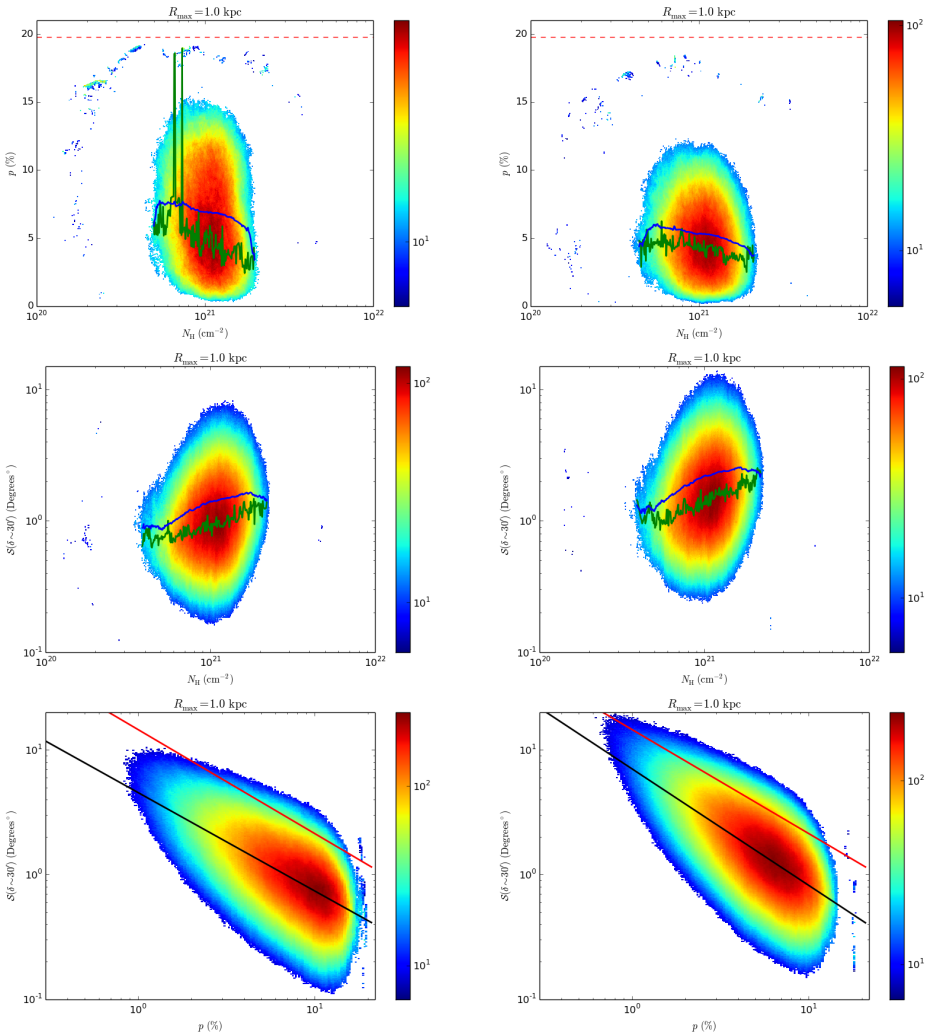

Fig. 10: Joint histograms of (*Top*) polarization fraction and column density, (*Middle*) polarization angle dispersion and column density, and (*Bottom*) polarization angle dispersion and fraction. Red line depicts the fit to the observations as presented in Planck Collaboration Int. XIX (2015), $\log_{10}\mathcal{S} = \alpha \log_{10} p + \beta$. Black lines are the best fits to our simulated data, to which α and β are given in the Table 2. Green lines follow the maximum counts in the histograms as a function of $N_{\rm H}$, and blue lines present a weighted mean of the polarization fractions. *Left:* Normal case. *Right:* Doubled perturbations case. In all cases $R_{\rm max} = 1$ kpc.

Note, that $B_0\hat{\mathbf{y}}$ here is distinct from $\bar{\mathbf{B}}$ as defined in Eq. (1), which is defined by local averaging and includes varying x and y components, although most strongly aligned along y. In the MHD model the fluctuations $\mathbf{b}$ have the same order of magnitude as $\bar{\mathbf{B}}$, which complicates visualising the large scale mean field even with the simulated observations. For observations the structure of the mean field is even more opaque, as the mean field direction is subject to large scale diversions when interracting with spiral arms and the central bulge of the galaxy. Therefore, using this interpretation to understand the observed $\mathcal{S}$ by PlanckXIX is not trivial. In the case of our MHD simulation, the mean field is clearly stronger than the fluctuating field. In the case of our Galaxy, the general structure of the large-scale field is more complicated and the fluctuations are stronger (e.g. Rand & Kulkarni 1989; Haverkorn 2015). More importantly, calculating the polarization angle from weakly polarized emission is prone to large errors (Montier et al. 2015; Alina et al. 2016), which will show up as artificial angular dispersion due to measurement noise. However, PlanckXIX state that especially with high values of $\mathcal{S}$ the effect of bias is small, so the effect of large-scale magnetic field on $\mathcal{S}$ could encourage further study.

4.3. Effect of magnetic fluctuations

To assess the relevance of the mean and fluctuation field to the simulated observations, we explore the impact of increasing the strength of the fluctuations relative to the mean field. Using the decomposition of the field as illustrated in Fig. 2, we double the fluctuation component of the magnetic field and then sum it with the mean field to obtain a physically generated field with stronger fluctuations.

Doubling the perturbed field strength somewhat reduces p and increases $\mathcal{S}$, as can be seen by comparing between the left and right joint histograms in the top two rows of Fig. 10. The column density is not affected, understandable as the thermodynamic properties of the model are unchanged. The trends in maximum count and weighted mean, traced on the histograms by the green and blue lines, respectively, do not change, but they shift correspondingly with the general shift in the distribution. Comparing the joint histograms of $\mathcal{S}$ and p in the last row of Fig. 10, the log fit relating $\mathcal{S}$ to p in the simulation shifts marginally closer to the PlanckXIX fit, but the gradient of the line steepens. In this sense the original MHD still better explains

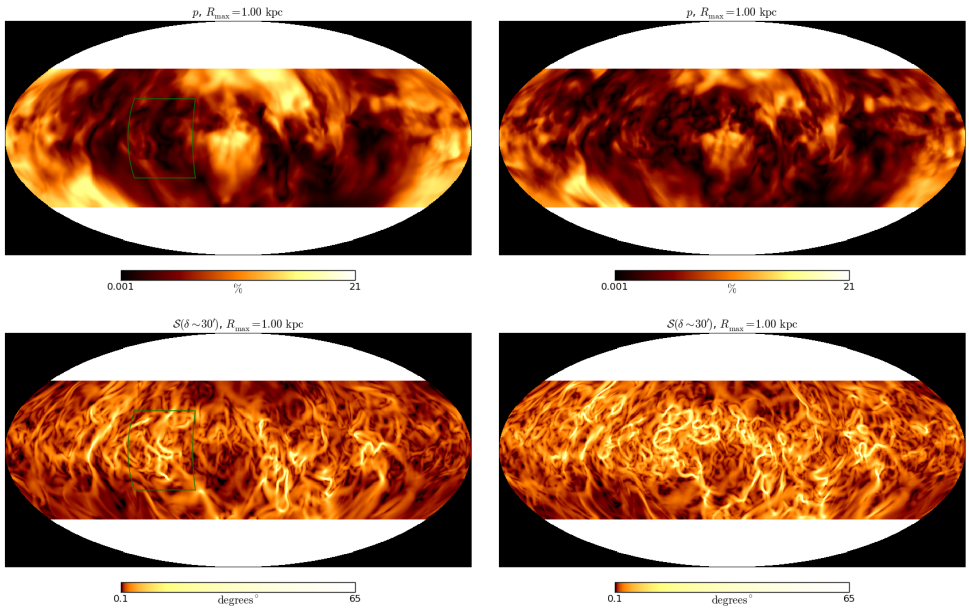

Fig. 11: *Top:* Sample maps of polarization fraction p. *Bottom:* Sample maps of polarization angle dispersion $\mathcal{S}$. *Left:* Normal case. *Right:* Doubled perturbations case. In all cases $R_{\rm max} = 1$ kpc,.

the relationship between $\mathcal{S}$ and p. The increases in $\mathcal{S}$ for the doubled perturbations is associated mainly with low values of p, while $\mathcal{S}$ associated with high $p \gtrsim 10\%$ remain less affected by the increased perturbations.

From the maps of p in Fig. 11 (top row) the polarization fraction is in general not only dampened, but also exhibits increasingly fine structure. This is also evident for $\mathcal{S}$ (bottom row), in which the filamentary structure for the doubly perturbed field (right) is highly fractured, compared to the map for the original field.

Increasing the relative strength of the fluctuations in the magnetic field does not bring us visibly closer to the $\mathcal{S}$ values observed by PlanckXIX. Nor can longer integration distance address this, although this does help with increasing column densities. The distribution of polarization fraction in the MHD simulations is spread slightly higher than in PlanckXIX, but doubling the strength of the random field component makes this a very good fit to PlanckXIX. Part of the contribution to $\mathcal{S}$ comes from the mean field, which in the MHD model is far from uniform. In the Galaxy, spiral arms and the central bulge will add to the variations in the mean field. Inclusion of such features in an MHD model would serve to enhance dispersion angles, but most likely the strongest factor is the limiting scale of the magnetic field fluctuations and gas density concentrations. These are truncated at the grid scale of 4 pc.

Given the long computation times as well as the large scales necessary to model SN driven dynamo, increased resolution in the near future is likely to be modest. Nevertheless the trends and characteristics exhibited with these simulations have much in common with the PlanckXIX results. Exploration of these simulated observations has helped to reveal how different aspects of the magnetic field contribute to the observations. A sweep of integration lengths $R_{\rm max}$, comparing observations from many viewing angles, and comparing results across even a limited range of MHD model resolution may offer further valuable insights.

5. Discussion and conclusions

In this paper, using MHD models supplemented with radiative transfer computations, we set out to study the effect on the polarization of dust in the ISM of the following physical ingredients:

- SN regulated multiphase ISM, with hot component, and with longitudinal and latitudinal anisotropy.
- The presence of ubiquitous shock fronts driven by SNe.
- The presence of self-consistently generated inhomogeneous and anisotropic magnetic fields both by large- and small-scale dynamos.

Previous investigations have been limited to the two-phase ISM, including only the cold molecular and diffuse warm gas components, with no or artificially induced shock fronts, and with imposed magnetic field configurations.

We find a very good correspondence with the simulated $\mathcal{S}$ maps, exhibiting a strongly filamentary structure, and the all-sky observations of PlanckXIX implying that our MHD models capture some essential features related to their formation. In accordance with the observations, we find a good match to the anticorrelation between polarization fraction p and polarization dispersion angle $\mathcal{S}$. The power law relation is quite accurately reflected in the simulation, although $\mathcal{S}$ differs by a factor 1/3, because it is sensitive to small scale fluctuations and the cold dense clouds, which the MHD model cannot sufficiently resolve.

The mean magnetic field has both a systematic orientation in the direction of the galactic shear and a non-uniform structure. This significantly affects the observed polarization properties. A strong plane-of-sky (POS) mean field is found to dominate over the small-scale component contribution to the polarization angles in such a way that the observed $\mathcal{S}$ is reduced. Correspondingly, when the mean field is parallel to the line-of-sight (LOS), the observed polarization angles are more sensitive to the small-scale fluctuations. Due to its varying orientation, the mean field also partially contributes to the generation of $\mathcal{S}$ filaments.

In addition to these general findings, our more detailed key results can be listed as follows:

- We have demonstrated a means to probe the relationship between the observations and the physical features along the LOS by varying the integration length ($R_{\rm max}$) in radiative transfer calculations.
- Periodic repeat sampling facilitates extending $R_{\rm max}$ along the LOS, beyond the horizontal size of the MHD models to retrieve more realistic column densities $N_{\rm H}$.
- Increasing $R_{\rm max}$ above 1 kpc increases $N_{\rm H}$ and reduces p in line with observed distributions, suggesting that there is a minimum value for $R_{\rm max}$ which is needed for simulated observations. However, to exclude artificial artefacts, we have to limit $R_{\rm max} \lesssim 2L_x$, where L_x is the model horizontal extent.
- p is correlated with the strength of the mean field in the POS and $\mathcal{S}$ is correlated positively with the fluctuating field **b** and inversely with p.
- Filamentary structure of $\mathcal{S}$ becomes smaller scale, brighter and more fragmentary with increasing $R_{\rm max}$, because there is more depolarization. The filaments are not correlated to the shock profiles in the ISM.
- We confirm the inverse correlation of $\mathcal{S}$ with p of the form $\log_{10}\mathcal{S} = \alpha \log_{10} p + \beta$. Supposing **b** to be approximately isotropic, it may be possible to apply this to the measurements of $\mathcal{S}$ and p to make inferences about the strength and orientation of the mean field.
- We compare simulated polarization observations here and in PlanckXX with Planck observations. The evidence supports a view that magnetic fields in and around molecular clouds are likely highly coherent, and oriented in the direction of the ambient magnetic field, in which it is located.

For future work, MHD models with increased resolution and/or horizontal extent to probe the effects of longer integration ranges and higher densities and fluctuations on $\mathcal{S}$ and $N_{\rm H}$ would be helpful. As these are essential for many scientific priorities, these opportunities will undoubtedly be fulfilled. Even with the current simulations the role of the fluctuating magnetic field can be further investigated by retaining the existing MHD field and adding to this an appropriate isotropic fluctuating field of the correct magnitude with disturbances at various smaller scales. Another way forward would be to use the saturated stages of the MHD models, re-mesh them to include denser grids and thereby finer scales, and re-run only up to a new saturated stage, eliminating the long dynamo evolutionary stage.

Conducting a series of experiments probing a range of $R_{\rm max}$ to analyse how physical features are being captured by the simulated observations in relation to the POV would shed more light on how polarization features are connected with the magnetic field structure. Including spiral arms in MHD simulations and exploring how this impacts on the structure of the magnetic field and anisotropy in the simulatied polarization observations could improve the interpretation of model results in terms of the Milky Way galaxy. Yet another possibility is to focus on zoomed-in features of the MHD models with similarities to the observed features from Planck, and this way to explore what we can learn about the 3D structure of the magnetic field at that location.

The often used Chandrasekhar-Fermi method (Chandrasekhar & Fermi 1953) allows for the determination of the POS magnetic field strength if the dispersion of polarization angle is known. It is especially useful for estimating magnetic field strengths in regions, such as molecular clouds, where the Zeeman effect is weak. An important direction of future work is to test the predictions of this method against the self-consistently generated large- and small-scale fields, ideally when the models can be refined to reach the limit where both of the quantities resemble their observed counterparts.

As we have shown in this paper, the interplay of the large- and small-scale magnetic fields can cause systematic effects in the polarization measures, that may well be used to map the mean magnetic field of the Milky Way. The ratio of $\mathcal{S}$ and p, reacting to the presence of different levels and orientations of the magnetic field components, may be used as a tracer of the orientation of the mean field, and on the other hand of the ratio of the strengths between large- and small-scale magnetic fields.

Acknowledgements. MSV, FAG, and MJK acknowledge support of the Grand Challenge project SNDYN, CSC-IT Center for Science Ltd. (Finland) and the Academy of Finland Centre of Excellence ReSoLVE (project number 272157). MJ acknowledges the support of the Academy of Finland Grant No. 250741. MSV acknowledges a grant from the Jenny and Antti Wihuri Foundation. Some of the results in this paper have been derived using the `HEALPix` package. This research has made use of NASA's Astrophysics Data System.

References

Abbott, D. C. 1982, ApJ, 263, 723
Alina, D., Montier, L., Ristorcelli, I., et al. 2016, A&A, 595, A57
Beck, R. 2016, A&A Rev., 24, 4
Bendre, A., Gressel, O., & Elstner, D. 2015, Astronomische Nachrichten, 336, 991
Bethell, T. J., Chepurnov, A., Lazarian, A., & Kim, J. 2007, ApJ, 663, 1055
Chandrasekhar, S. & Fermi, E. 1953, ApJ, 118, 113
Chen, C.-Y., King, P. K., & Li, Z.-Y. 2016, ApJ, 829, 84
Chevalier, R. A. 1977, ARA&A, 15, 175
Draine, B. T. & Weingartner, J. C. 1996, ApJ, 470, 551
Elmegreen, B. G. & Scalo, J. 2004, ARA&A, 42, 211
Evirgen, C. C., Gent, F. A., Shukurov, A., Fletcher, A., & Bushby, P. 2017a, in preparation
Evirgen, C. C., Gent, F. A., Shukurov, A., Fletcher, A., & Bushby, P. 2017b, MNRAS, 464, L105
Falceta-Gonçalves, D., Lazarian, A., & Kowal, G. 2008, ApJ, 679, 537
Ferrière, K. M. 2001, Reviews of Modern Physics, 73, 1031
Gent, F. A. 2012, PhD thesis, Newcastle University School of Mathematics and Statistics
Gent, F. A., Shukurov, A., Fletcher, A., Sarson, G. R., & Mantere, M. J. 2013a, MNRAS, 432, 1396
Gent, F. A., Shukurov, A., Sarson, G. R., Fletcher, A., & Mantere, M. J. 2013b, MNRAS, 430, L40
Haverkorn, M. 2015, in Magnetic Fields in Diffuse Media, ed. A. Lazarian, E. M. de Gouveia Dal Pino, & C. Melioli (Berlin: Springer), 483
Hennebelle, P., Banerjee, R., Vázquez-Semadeni, E., Klessen, R. S., & Audit, E. 2008, A&A, 486, L43
Hennebelle, P. & Iffrig, O. 2014, A&A, 570, A81
Hildebrand, R. H., Kirby, L., Dotson, J. L., Houde, M., & Vaillancourt, J. E. 2009, ApJ, 696, 567
Hollins, J. F., Sarson, G. R., Shukurov, A., Fletcher, A., & Gent, F. A. 2017, ArXiv e-prints [arXiv:1703.05187]
Juvela, M. 2005, A&A, 440, 531
Kim, C.-G. & Ostriker, E. C. 2015, ApJ, 815, 67
Klein, U. & Fletcher, A. 2015, Galactic and Intergalactic Magnetic Fields
Lamarre, J.-M., Puget, J.-L., Ade, P. A. R., et al. 2010, A&A, 520, A9
Lozinskaya, T. A. 1992, Supernovae and stellar wind in the interstellar medium
Mathis, J. S., Mezger, P. G., & Panagia, N. 1983, A&A, 128, 212
McKee, C. F. & Ostriker, J. P. 1977, ApJ, 218, 148
Montier, L., Plaszczynski, S., Levrier, F., et al. 2015, A&A, 574, A135
Ostriker, E. C., Stone, J. M., & Gammie, C. F. 2001, ApJ, 546, 980
Padoan, P., Goodman, A., Draine, B. T., et al. 2001, ApJ, 559, 1005
Pelkonen, V.-M., Juvela, M., & Padoan, P. 2009, A&A, 502, 833
Planck Collaboration Int. I. 2011, A&A, 536, A1
Planck Collaboration Int. XIX. 2015, A&A, 576, A104
Planck Collaboration Int. XX. 2015, A&A, 576, A105
Planck Collaboration Int. XXI. 2015, A&A, 576, A106
Planck Collaboration Int. XXII. 2015, A&A, 576, A107
Rand, R. J. & Kulkarni, S. R. 1989, ApJ, 343, 760
Soler, J. D., Hennebelle, P., Martin, P. G., et al. 2013, ApJ, 774, 128
Tammann, G. A., Löffler, W., & Schröder, A. 1994, ApJS, 92, 487
Vazquez-Semadeni, E. 1994, ApJ, 423, 681